Title

Spectral Galerkin solver for intense beam Vlasov equilibria in nonlinear constant focusing channels

Journal

Physical Review E, 100(5)

ISSN

2470-0045

Authors

Mitchell, Chad E

Ryne, Robert D

Hwang, Kilean

Publication Date

2019-11-01

DOI

10.1103/physreve.100.053308

Peer reviewed

Spectral Galerkin Solver for Intense Beam Vlasov Equilibria in Nonlinear Constant Focusing Channels

Chad E. Mitchell,* Robert D. Ryne, and Kilean Hwang
Lawrence Berkeley National Laboratory, Berkeley, CA 94720, USA
(Dated: October 21, 2019)

A numerical method is described for producing stationary solutions of the Vlasov-Poisson system describing a relativistic charged-particle beam in a constant focusing accelerator channel, confined transversely by a general (linear or nonlinear) focusing potential. The method utilizes a variant of the spectral Galerkin algorithm to solve a nonlinear PDE in two degrees of freedom for the beam space charge potential in equilibrium. Numerical convergence with increasing number of computed spectral modes is investigated for several benchmark problems. Preservation of the stationary phase space density is verified using a strongly nonlinear focusing channel based on the Integrable Optics Test Accelerator at Fermi National Accelerator Laboratory.

I. INTRODUCTION

In the study of intense charged particle beams in accelerator storage rings and circular colliders, a central problem is the construction of a periodically-varying beam phase space density with periodicity matched to the underlying accelerator structure. This is a challenging problem whose solution has implications for the long-term stability of the stored beam. Constant focusing models, which approximate the beam as a confined non-neutral plasma in a set of static focusing fields, remain the standard tool for studying the structure and stability of intense beam equilibria in such systems [1–5]. In the beam physics community, studies of such equilibria typically assume that the beam is confined by linear external focusing forces. With the exception of singular KV-type equilibria [6, 7], such studies have also assumed rotational symmetry about the direction of the beam centroid motion. A small number of authors have considered the case of nonlinear focusing forces with this symmetry [8, 9]. In this paper, we describe a numerical method for producing families of beam equilibria in a general nonlinear focusing potential in two degrees of freedom, without symmetry restrictions. Special attention is given to the Hamiltonian structure of the particle equations of motion.

In the case of an unbunched coasting beam, the search for such equilibria is equivalent to searching for stationary solutions of the nonlinear Vlasov-Poisson system. This system can profitably be reduced to a 2D semilinear elliptic PDE with an integral constraint, to be solved for the electrostatic potential of the beam self-fields in equilibrium. Existing algorithms for solving semilinear boundary-value problems may then be applied to solve this problem, after minor modification. In contrast to finite-element or finite-difference algorithms, spectral Galerkin algorithms provide a smooth (infinitely-differentiable) approximation to the solution, given as a linear combination of analytically-known global basis functions with good completeness and convergence properties. Knowledge of the linear coefficients is useful, for example, in studying individual charged-particle orbits in the equilibrium fields.

The layout of this paper is as follows. Section II provides a theoretical overview of intense beam equilibria in constant focusing channels, culminating in a PDE (15) to be solved for the equilibrium space charge potential. Section III describes a numerical algorithm for solution of this problem using a spectral Galerkin approach. Section IV describes details of our numerical implementation, while Section V describes code benchmarks and studies of numerical convergence. Section VI describes an application to a nonlinear focusing channel based on the Integrable Optics Test Accelerator at Fermi National Accelerator Laboratory. There are three brief appendices.

II. INTENSE BEAM EQUILIBRIA IN A CONSTANT FOCUSING CHANNEL

A. The Vlasov-Poisson System

Consider an axially uniform beam of identical particles with charge q and mass m moving with relativistic momentum $p^0 = mc\beta_0\gamma_0$ in the direction of coordinate s in a channel confined by a transverse focusing potential V_0 (generated by applied s-independent magnetostatic or electrostatic fields). Using s as the independent variable (time-like parameter), the collection of particles at each s is described by a probability density f on the 4D phase space (x, p_x, y, p_y), satisfying:

$$\int f(x, p_x, y, p_y, s) dx dp_x dy dp_y = 1, \qquad f \geq 0. \tag{1}$$

Here, we take the momenta p_x and p_y to be normalized by the design momentum p^0, and we assume $|p_x|$, $|p_y| << 1$. In the collisionless limit, the phase space density f evolves according to the Vlasov equation [1, 2]:

$$\frac{\partial f}{\partial s} + \{f, H\} = 0, \tag{2}$$

* ChadMitchell@lbl.gov

where

$$H = \frac{1}{2}(p_x^2 + p_y^2) + V_0(x,y) + \frac{q\phi(x,y,s)}{\beta_0^2\gamma_0^3 mc_0^2} \tag{3}$$

is the Hamiltonian of the particle motion, $\{\cdot,\cdot\}$ is the Poisson bracket, given explicitly by:

$$\{f,H\} = \left(\frac{\partial f}{\partial x}\frac{\partial H}{\partial p_x} - \frac{\partial f}{\partial p_x}\frac{\partial H}{\partial x}\right) + \left(\frac{\partial f}{\partial y}\frac{\partial H}{\partial p_y} - \frac{\partial f}{\partial p_y}\frac{\partial H}{\partial y}\right), \tag{4}$$

and ϕ is the space charge potential describing the beam self-fields, which satisfies the following 2D Poisson equation on the transverse domain Ω (the interior of the beam pipe):

$$\nabla^2\phi = -\frac{\rho}{\epsilon_0} \text{ in } \Omega, \qquad \phi|_{\partial\Omega} = 0. \tag{5}$$

Here $\partial\Omega$ denotes the boundary of Ω, and the charge density ρ at s is determined by the phase space density f through:

$$\rho(x,y,s) = q\lambda \int f(x,p_x,y,p_y,s)dp_x dp_y \tag{6}$$

for $(x,y) \in \Omega$, where λ denotes the number of particles per unit length. In the following sections, we search for equilibrium solutions of the system (2-6) for a specified confining potential V_0.

B. Constructing Stationary Distributions

We obtain a stationary solution of (2) satisfying $\partial f/\partial s = 0$ if and only if:

$$\{f,H\} = 0. \tag{7}$$

Such a solution can be constructed by taking $f_{eq} = G \circ H$ for some specified differentiable function $G : \mathbb{R} \to \mathbb{R}$, provided G is chosen so that (1) is satisfied. This follows from (7) since:

$$\{f_{eq}, H\} = \{G \circ H, H\} = G' \circ H\{H,H\} = 0. \tag{8}$$

For convenience, define the dimensionless quantities:

$$\Phi(x,y) = \frac{q\phi(x,y)}{\beta_0^2\gamma_0^3 mc_0^2}, \quad V(x,y) = V_0(x,y) + \Phi(x,y). \tag{9}$$

Then the spatial projection P_{xy} of the phase space density f_{eq} takes the form:

$$\begin{aligned} P_{xy}(x,y) &= \int_{-\infty}^{\infty}\int_{-\infty}^{\infty} f_{eq}(x,p_x,y,p_y)dp_x dp_y \\ &= \int_{-\infty}^{\infty}\int_{-\infty}^{\infty} G\left(\frac{1}{2}(p_x^2+p_y^2) + V(x,y)\right)dp_x dp_y \\ &= 2\pi\int_0^{\infty} G\left(\frac{p^2}{2} + V(x,y)\right)pdp \\ &= 2\pi\int_{V(x,y)}^{\infty} G(h)dh. \end{aligned} \tag{10}$$

Using (6) and (9) in the Poisson equation (5) gives that:

$$\nabla^2\Phi = -\left(\frac{\lambda q^2}{\beta_0^2\gamma_0^3 mc_0^2\epsilon_0}\right)P_{xy} = -2\pi K P_{xy}, \tag{11}$$

where

$$K = \frac{\lambda q^2}{2\pi\beta_0^2\gamma_0^3 mc_0^2\epsilon_0} = \frac{2I}{\beta_0^3\gamma_0^3 I_A} \tag{12}$$

is the generalized beam perveance, expressed in terms of the beam current I. Define a space charge intensity parameter $\Lambda = (2\pi)^2 K$. It follows by using (10) in (11) that the self-consistent space charge potential Φ of the stationary beam density f_{eq} must satisfy:

$$\nabla^2\Phi(x,y) = -\Lambda\int_{V(x,y)}^{\infty} G(h)dh, \qquad (x,y) \in \Omega \tag{13}$$

subject to the condition that $\Phi = 0$ on the boundary $\partial\Omega$. Note that the lower limit of the integral in (13) depends on Φ through (9).

To enforce the two conditions in (1), choose the function G to be nonnegative and put $G = f_0\tilde{G}$ for some constant $f_0 > 0$, to be determined. Define the indefinite integral:

$$G_{\text{int}}(h) = \int_h^{\infty} \tilde{G}(h')dh', \qquad h \in \mathbb{R}. \tag{14}$$

Using (14) in (13) then gives the nonlinear PDE:

$$\nabla^2\Phi = -\Lambda f_0 G_{\text{int}}(V_0 + \Phi) \text{ in } \Omega, \qquad \Phi|_{\partial\Omega} = 0. \tag{15a}$$

Likewise, using (14) in (10), the normalization condition (1) gives the integral constraint:

$$f_0 = \left(2\pi\int_\Omega G_{\text{int}}(V_0(x,y) + \Phi(x,y))dxdy\right)^{-1}. \tag{15b}$$

If a pair (Φ, f_0) satisfying (15) can be obtained, a stationary phase space density $f_{eq} = f_0\tilde{G} \circ H$ is obtained by using the fact that $H = ||p||^2/2 + V_0 + \Phi$, where $||p||^2 = p_x^2 + p_y^2$. In the following section, we describe a method for solving (15).

III. SOLVING THE PDE FOR THE EQUILIBRIUM POTENTIAL

Consider a nonlinear PDE of the form:

$$\nabla^2 U = F(\cdot, U) \quad \text{on} \quad \Omega, \qquad U|_{\partial\Omega} = 0, \tag{16}$$

for a specified function F and an unknown function U, to be determined. For example, equation (15a) takes the form (16) when the function F is given by:

$$F(x,y,U) = -\Lambda f_0 G_{\text{int}}(V_0(x,y) + U) \tag{17}$$

for $(x, y) \in \Omega$ and $U \in \mathbb{R}$. Given a reliable algorithm for solving the linear Poisson equation, one may attempt to solve (16) as follows. Set $U^{(0)} = 0$ and solve, for $r = 0, 1, 2, \ldots$:

$$\nabla^2 U^{(r+1)} = F(\cdot, U^{(r)}) \text{ on } \Omega, \quad U^{(r+1)}\Big|_{\partial\Omega} = 0. \tag{18}$$

For each r, compute the difference $\Delta^{(r)} = ||U^{(r+1)} - U^{(r)}||$ in a convenient norm, and halt when $\Delta^{(r)} < \epsilon$, where ϵ denotes the desired tolerance, indicating numerical convergence. In the special case that F is given by (17) for well-behaved G_{int}, this procedure can be shown to converge when the intensity Λ is sufficiently small. At high intensity, a different procedure is required.

We use the spectral Galerkin procedure described in [10, 11]. Let $\{e_j : j = 1, 2, \ldots\}$ denote an orthonormal basis of $L^2(\Omega)$ consisting of smooth real-valued eigenfunctions of the Laplacian on the domain Ω with eigenvalues λ_j, so that for $j = 1, 2, 3, \ldots$:

$$\nabla^2 e_j = \lambda_j e_j, \qquad e_j|_{\partial\Omega} = 0, \qquad \lambda_{j+1} \leq \lambda_j < 0. \tag{19}$$

This set of eigenfunctions is guaranteed to exist for any bounded, open subset $\Omega \subset \mathbb{R}^d$ $(d = 1, 2, \ldots)$ [12]. We search for $U_n \in \text{Span}\{e_1, e_2, \ldots, e_n\}$ such that U_n is an approximate solution of (16), in the following sense. Let the residual $R_n = \nabla^2 U_n - F(\cdot, U_n)$ denote the difference between the left and right-hand sides of (16), and let $\langle \cdot, \cdot \rangle$ denote the inner product on $L^2(\Omega)$. It is required that:

$$\langle R_n, e_i \rangle = 0, \qquad 1 \leq i \leq n, \tag{20}$$

so that R_n is orthogonal to the subspace $\text{Span}\{e_1, e_2, \ldots, e_n\}$. Informally, U_n must satisfy (16) accurately for all modes through those of index n.

Define a map $\mathcal{T} : \mathbb{R}^n \to \mathbb{R}^n$ given by $\mathcal{T}(\alpha) = \alpha^f$, where for $1 \leq i \leq n$

$$\alpha_i^f = \int_\Omega e_i(x, y) F\left(x, y, \sum_{j=1}^n \frac{\alpha_j}{\lambda_j} e_j(x, y)\right) dxdy. \tag{21}$$

Given a point $\alpha \in \mathbb{R}^n$ with $\mathcal{T}(\alpha) = \alpha$ (a fixed point of $\mathcal{T}$), an approximate solution U_n of (16) is given by:

$$U_n = \sum_{j=1}^n \frac{\alpha_j}{\lambda_j} e_j. \tag{22}$$

To see this, note that it follows by using (19) in (22) that:

$$\nabla^2 U_n = \sum_{j=1}^n \alpha_j e_j, \qquad U_n|_{\partial\Omega} = 0. \tag{23}$$

In particular, U_n satisfies the desired boundary condition. Using the fact that the e_j are orthonormal gives:

$$\langle \nabla^2 U_n, e_i \rangle = \alpha_i, \qquad 1 \leq i \leq n. \tag{24}$$

Likewise, using (22) and the definition of the inner product gives:

$$\begin{aligned} \langle F(\cdot, U_n), e_i \rangle &= \int_\Omega e_i(x, y) F(x, y, U_n(x, y)) dxdy \qquad (25) \\ &= \int_\Omega e_i(x, y) F\left(x, y, \sum_{j=1}^n \frac{\alpha_j}{\lambda_j} e_j(x, y)\right) dxdy \\ &= \alpha_i, \qquad 1 \leq i \leq n, \end{aligned}$$

where in the last equality we used the fact that α is a fixed point of (21). Thus, letting $R_n = \nabla^2 U_n - F(\cdot, U_n)$ we have for each $1 \leq i \leq n$ that:

$$\langle R_n, e_i \rangle = \langle \nabla^2 U_n, e_i \rangle - \langle F(\cdot, U_n), e_i \rangle = 0, \tag{26}$$

as desired.

An analysis of the numerical error of this procedure and the convergence of U_n with increasing n is provided in [10, 11]. The existence and uniqueness of solutions to (16) both depend strongly on the properties of the function F, and a general discussion is beyond the scope of this paper. See, for example, the discussions in [10, 13, 14].

A. Application to Vlasov Equilibria

To apply this procedure to solve (15), let $\tilde{G}$ denote a (unitless) desired functional form of G, with $\tilde{G} \geq 0$, and choose a convenient scale length $L > 0$. An approximate solution of (15) is obtained by searching for a zero $\alpha \in \mathbb{R}^{n+1}$ of the map $\mathcal{M} : \mathbb{R}^{n+1} \to \mathbb{R}^{n+1}$, where $\alpha = (\alpha_0, \alpha_1, \ldots, \alpha_n)$ and $\mathcal{M}(\alpha)$ has the (unitless) components:

$$\begin{aligned} [\mathcal{M}(\alpha)]_i &= -\alpha_i L \qquad (27a) \\ &- \Lambda\alpha_0 \int_\Omega e_i(x, y) G_{\text{int}}\left(V_0(x, y) + \sum_{j=1}^n \frac{\alpha_j}{\lambda_j} e_j(x, y)\right) dxdy, \\ [\mathcal{M}(\alpha)]_0 &= -1 \qquad (27b) \\ &+ \frac{2\pi\alpha_0}{L} \int_\Omega G_{\text{int}}\left(V_0(x, y) + \sum_{j=1}^n \frac{\alpha_j}{\lambda_j} e_j(x, y)\right) dxdy, \end{aligned}$$

where $1 \leq i \leq n$. Given a point $\alpha \in \mathbb{R}^{n+1}$ with $\mathcal{M}(\alpha) = 0$, we obtain an approximate solution Φ_n of (15), together with an equilibrium phase space density f_{eq} and its associated spatial projection P_{xy} by:

$$\Phi_n = \sum_{j=1}^n \frac{\alpha_j}{\lambda_j} e_j, \qquad f_0 = \frac{\alpha_0}{L}, \tag{28a}$$

$$f_{eq} = f_0(\tilde{G} \circ H_n), \qquad P_{xy} = 2\pi f_0(G_{\text{int}} \circ V_n), \tag{28b}$$

$$H_n = \frac{||p||^2}{2} + V_n, \qquad V_n = V_0 + \Phi_n. \tag{28c}$$

To verify that the solution (28) has the desired properties, note that putting $f_0 = \alpha_0/L$ in (17) gives:

$$F(x, y, \Phi_n(x, y)) = -\frac{\Lambda\alpha_0}{L} G_{\text{int}}(V_0(x, y) + \Phi_n(x, y)). \tag{29}$$

Integrating (29) against the n basis functions $\{e_i : i = 1, \ldots, n\}$ and using the first n equations in (27) demonstrates that $(\alpha_1, \ldots, \alpha_n) \in \mathbb{R}^n$ is a fixed point of the map (21), so that Φ_n is an approximate solution of (15a). More precisely, the residual $R_n = \nabla^2\Phi_n - F(\cdot, \Phi_n)$ satisfies the condition (20). Likewise, the final equation in (27) yields:

$$f_0 = \frac{\alpha_0}{L} = \left(2\pi \int_\Omega G_{\text{int}}(V_0(x, y) + \Phi_n(x, y))dxdy\right)^{-1}, \tag{30}$$

so the normalization condition (15b) is also satisfied.

Note that the parameter L is introduced to provide consistency of units among the components of α. By varying L one may adjust the relative weight, within the search for zeros of $\mathcal{M}$, of the fixed point condition (21) required for solving (15a) and enforcement of the normalization condition (15b).

IV. NUMERICAL IMPLEMENTATION

The procedure described in the previous section has been implemented as a parallel Fortran 90+MPI code for computing stationary solutions of the Vlasov-Poisson system (2-6). For a given focusing potential V_0 and a given function G, the code returns the solution of (15) for the equilibrium space charge potential Φ, the coefficients of Φ in the basis (19), and a set of N_p particles sampled from the 4D phase space density $f_{eq} = G \circ H$. Table I lists the numerical input and output.

For this implementation, we assume a rectangular conducting beam pipe, so the domain is given by $\Omega = (-a, a) \times (-b, b)$. The basis functions in (19) and their corresponding eigenvalues are then given explicitly by:

$$e_{l,m}(x, y) = \frac{1}{\sqrt{ab}} \sin\left(\frac{l\pi}{2a}(x + a)\right) \sin\left(\frac{m\pi}{2b}(y + b)\right), \tag{31a}$$

$$\lambda_{l,m} = -\left(\frac{l\pi}{2a}\right)^2 - \left(\frac{m\pi}{2b}\right)^2, \qquad l, m = 1, 2, \ldots \tag{31b}$$

For bookkeeping purposes, the coefficients of the modes (l, m) are stored and manipulated in a 1D array, with ordering given by the single index $j(l, m) = (l - 1)m_{max} + m$. Consistent with the notation of the previous section, the 1D mode index j satisfies $1 \le j \le n$ with $n = l_{max}m_{max}$. The code could easily be modified to treat the case of a round beam pipe by replacing the functions (31) by the eigenfunctions of the Laplacian in a circular disk.

The primary components of the algorithm are as follows. To search for zeros of the map $\mathcal{M} : \mathbb{R}^{n+1} \to \mathbb{R}^{n+1}$ given by (27), Broyden's method [15, 16] for nonlinear root finding is applied. At each iteration of Broyden's method, numerical integration of the 2D integrals appearing in (27) is achieved by partitioning Ω into square cells, and using a 7-point cubature formula on each cell that is exact for polynomials through degree 5 [17]. Within the integrand, the basis functions and eigenvalues are given by (31). Once a zero $\alpha \in \mathbb{R}^{n+1}$ is obtained, a solution for the potential Φ_n is given by (28). Particles are sampled from the equilibrium phase space density f_{eq} using a rejection method in 5D. A point (x, p_x, y, p_y, u) is sampled from a uniform probability density within a 5D box. If $u > f_{eq}(x, p_x, y, p_y)$, then the point is rejected. Otherwise, the point is retained. This procedure is repeated until N_p points have been retained.

The code produces several diagnostic quantities to check the quality of the numerical solution. These include the norm $||\mathcal{M}(\alpha)||$, to check the quality of the nonlinear root-finding, the residual R_n, given by the difference between the left-hand and right-hand sides of the PDE (15a), and its norm $||R_n||$ in $L^2(\Omega)$. The latter quantity is used to characterize the global numerical error. Note that R_n must satisfy (20) by construction, provided that the root-finding is successful.

TABLE I. Numerical input and output for the spectral Galerkin code described in Section IV.

Code Input
a, b - half-aperture of the rectangular domain
l_{max}, m_{max} - number of horizontal and vertical modes
n_x, n_y - number of points used in the 2D integrals (27)
ϵ - tolerance threshold for numerical root-finding
Λ - space charge intensity parameter
N_p - number of sampled particles desired
parameters specifying the external potential V_0
parameters specifying the function G
initial guess for the coefficients $(\alpha_0, \ldots, \alpha_n)$ in (27)
Code Ouput
final value of $||\mathcal{M}(\alpha)||$ (should be $< \epsilon$)
integral of the spatial density P_{xy} (should be 1)
final values of the coefficients $(\alpha_0, \ldots, \alpha_n)$ in (27)
solution on a 2D grid $(x, y, \Phi(x, y), P_{xy}(x, y), R_n(x, y))$
norm of the residual error $||R_n||$ in $L^2(\Omega)$
quadratic part of $V = V_0 + \Phi$ at the origin
file of N_p particles (x, p_x, y, p_y) sampled from f_{eq}

A. Parallelization

When high numerical resolution is required, both the number of desired modes n and the number of desired particles N_p may be large. In order to treat this situation

the code is parallelized with MPI. Since the coefficients of the spectral modes can be calculated independently, we have each MPI process evaluate a fraction of those coefficients. Then the coefficients are broadcast to all processes with an MPI_ALLREDUCE operation. In order to generate a numerical distribution we use a particle decompostion in which each MPI process contains a fraction of the particles. The previously mentioned rejection method (with a unique random number seed) is then used by each process to generate its particles.

V. NUMERICAL BENCHMARKS

Suppose we desire a problem of the form (15) with an exactly-known solution. Let P_d be an exactly-known probability density on the domain Ω, and let Φ_d be an exactly-known solution of the linear Poisson equation:

$$\nabla^2\Phi_d = -\frac{\Lambda}{2\pi}P_d \quad \text{on} \quad \Omega, \qquad \Phi_d|_{\partial\Omega} = 0. \tag{32}$$

Let $R \subseteq \mathbb{R}$ denote the range of the function $G_{\rm int}$. If the function $G_{\rm int}$ is injective, with inverse $G_{\rm int}^{-1} : R \to \mathbb{R}$ defined on its range, one may define an applied potential V_0 of the form:

$$V_0(x,y) = G_{\rm int}^{-1}\left[\frac{P_d(x,y)}{2\pi f_0}\right] - \Phi_d(x,y), \tag{33}$$

where $(x,y) \in \Omega$ and $f_0 > 0$, provided the term in brackets $[\cdot]$ takes values in R, so that (33) is defined. It follows by direct substitution that $\Phi = \Phi_d$ is an exact solution of the nonlinear PDE (15a) with V_0 given by (33), which correctly satisfies the integral constraint (15b). Furthermore, the spatial projection of the stationary phase space density f_{eq} is given explicitly by $P_{xy} = P_d$.

Appendix B describes two such exactly soluble problems, which were studied for several values of the problem parameters Λ, H_0, a, and b. As measures of global relative numerical error, we use the two quantities:

$$E_n^{(1)} = \frac{||\Phi_n - \Phi_d||}{||\Phi_d||}, \qquad E_n^{(2)} = \frac{||R_n||}{||\nabla^2\Phi_d||}. \tag{34}$$

Here Φ_n is the approximate solution (28) obtained using n modes, and Φ_d is the exactly-known solution. The quantity $E_n^{(2)}$ measures the size of $R_n = \nabla^2\Phi_n - F(\cdot,\Phi_n)$ with F given by (29), which is the residual characterizing the difference between the left-hand and right-hand sides of the PDE. For simplicity, we take $a = b$ and $l_{max} = m_{max}$, so that the total number of computed modes is $n = l_{max}^2$. Figure 1 shows the decay of $E_n^{(1)}$ and $E_n^{(2)}$ with increasing l_{max} for both problems, illustrating convergence to the exact solution in each case.

For large n, the rates of decay of $E_n^{(1)}$ and $E_n^{(2)}$ are well-described by the rates of convergence of the Fourier series for Φ_d and $\nabla^2\Phi_d$, respectively. More precisely, if we define:

$$\Phi_n^{\rm trunc} = \sum_{j=1}^{n}\langle\Phi_d, e_j\rangle e_j, \qquad n = 1,2,3,\ldots \tag{35}$$

then for large n we observe that $E_n^{(1)}$ and $E_n^{(2)}$ satisfy to high precision:

$$E_n^{(1)} \approx \frac{||\Phi_n^{\rm trunc} - \Phi_d||}{||\Phi_d||}, \quad E_n^{(2)} \approx \frac{||\nabla^2\Phi_n^{\rm trunc} - \nabla^2\Phi_d||}{||\nabla^2\Phi_d||}. \tag{36}$$

For the problems described by potentials $V_0^{(I)}$ and $V_0^{(II)}$ of Appendix B, the asymptotic behavior of the quantities in (36) can be evaluated exactly in the limit $l_{max} \to \infty$, to give the following error estimates when $a = b$:

$$E_n^{(1,I)} \sim \frac{8\sqrt{3}}{\pi^3}l_{max}^{-5/2}, \qquad E_n^{(2,I)} \sim \frac{2}{\pi}\sqrt{\frac{6}{11}}l_{max}^{-1/2} \tag{37a}$$

$$E_n^{(1,II)} \sim \frac{\pi^3}{24\sqrt{15d}}l_{max}^{-9/2}, \qquad E_n^{(2,II)} \sim \frac{8\sqrt{3}}{\pi^3}l_{max}^{-5/2} \tag{37b}$$

which appear as the solid lines in Fig. 1. (The exact value of the coefficient $d \approx 1/4$ appearing in (37b) is given in Appendix B.) From (37) we see that $E_n^{(1)} \sim O(l_{max}^{-2})E_n^{(2)}$ for both problems. Numerical convergence occurs most slowly near the computational boundary due to Gibbs effects.

The rate of numerical convergence is improved when P_{xy} is smooth and localized away from the boundary, due to rapid convergence of the spectral series. As an example, consider the potential

$$V_0^{(III)}(x,y) = \frac{1}{2}k^2(x^2+y^2) + \frac{t}{3}(x^3 - 3xy^2). \tag{38}$$

The contour curves of (38) are closed for all values less than $H_{esc} = k^6/(6t^2)$. We compute a stationary smooth-edged waterbag distribution (Appendix A) with $H_0 = H_{esc}/2$ and $\lambda = 0.1$. The exact solution of (15) for this potential is unknown when $\Lambda \neq 0$. Figure 2 illustrates the computed spatial density P_{xy} and the residual $E_n^{(2)}$, together with the remaining problem parameters. In computing $E_n^{(2)}$, we use $\Phi_d \approx \Phi_n$ for $n = 35\times35$. Note that $E_n^{(2)}$ exhibits exponential decay with increasing l_{max} for the range of numerical parameters considered here.

VI. APPLICATION TO A NONLINEAR FOCUSING CHANNEL

As a challenging and physically relevant example, we consider an intense beam confined by a strongly nonlinear focusing potential similar to that used in the Integrable Optics Test Accelerator at Fermi National Accelerator

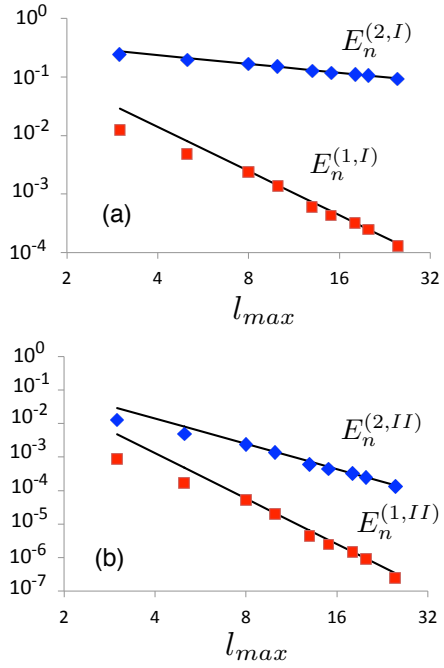

FIG. 1. Two measures of global relative numerical error (34) are shown for computed solutions of the exactly-soluble test problems associated with potentials $V_0^{(I)}$ (upper, panel a) and $V_0^{(II)}$ (lower, panel b) of Appendix B. Solid lines denote the corresponding error estimates given in (37), which are valid for large l_{max}.

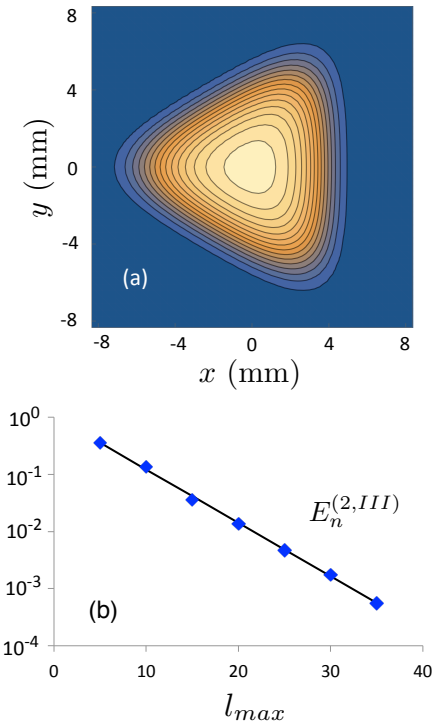

FIG. 2. (Upper, panel a) Contours of the spatial projection P_{xy} of a stationary waterbag phase space density f_{eq} obtained for a 2.5 MeV proton beam with current $I = 60.7$ mA in a constant focusing channel described by (38) with $k = 0.785$ m^{-1} and $t = 32.8$ m^{-3}. The domain boundary is located at $a = b = 1.69$ cm. (Lower, panel b) Decay of global relative numerical error for the problem (38). The solid line is a fit showing exponential decay with increasing l_{max}.

Laboratory [18, 19]. Consider a constant focusing channel (3) in which motion is described by the Hamiltonian:

$$H(x, p_x, y, p_y, s) = \frac{1}{2}(p_x^2 + p_y^2) + V_0(x, y) + \Phi(x, y, s), \tag{39a}$$

where the applied potential V_0 takes the form:

$$V_0(x, y) = \frac{1}{2}k^2(x^2 + y^2) - \frac{\tau c^2}{\beta}\mathcal{U}\left(\frac{x}{c\sqrt{\beta}}, \frac{y}{c\sqrt{\beta}}\right). \tag{39b}$$

Here $k = 1/\beta$, β [m], c [m$^{1/2}$], and τ [unitless] are constants, and $\mathcal{U}$ is the function:

$$\mathcal{U}(\zeta, \eta) = \mathcal{R}e\left(\frac{z}{\sqrt{1 - z^2}}\arcsin(z)\right), \quad z = \zeta + i\eta. \tag{39c}$$

It is convenient to define the dimensionless quantities:

$$V_N = \frac{\beta}{c^2}V_0, \qquad x_N = \frac{x}{c\sqrt{\beta}}, \qquad y_N = \frac{y}{c\sqrt{\beta}}, \tag{40}$$

in terms of which (39b) takes the simpler form:

$$V_N(x_N, y_N) = \frac{1}{2}(x_N^2 + y_N^2) - \tau\mathcal{U}(x_N, y_N). \tag{41}$$

We compute thermal stationary solutions of the Vlasov-Poisson system (2-6) associated with (39) by solving the PDE (15) with $G_{\rm int}(h) = H_0\exp(-h/H_0)$ in the domain $(x_N, y_N) \in (-1.5, 1.5) \times (-1.5, 1.5)$.

Consider a proton beam with a kinetic energy of $(\gamma_0 - 1)mc^2 = 2.5$ MeV and beam current of $I = 60.7$ mA. The beam is assumed to propagate in a focusing channel described by (39) with $\tau = -0.4$, $c = 0.01$ m$^{1/2}$, and $\beta = 1.27$ m. The transverse half-aperture of the beam pipe is given by $a = b = 1.69$ cm. The parameter H_0 is chosen to produce a distribution with normalized rms emittances $\epsilon_{x,n} = 0.4$ μm and $\epsilon_{y,n} = 0.8$ μm, where $\epsilon_{x,n} = \beta_0\gamma_0\sqrt{\langle x^2\rangle\langle p_x^2\rangle - \langle xp_x\rangle^2}$, with a similar expression for $\epsilon_{y,n}$ [1].

Figure 3 shows the applied potential (41) together with contours of the spatial density P_{xy} of an equilibrium beam computed using 15×15 modes ($l_{max} = m_{max} = 15$). Note the presence of singular points at $(x_N, y_N) = (\pm 1, 0)$, which provide strong horizontal confinement. Figure 4 shows the relative size of the residual R_n of the computed solution Φ_n for the equilibrium potential. This quantity is largest near the singular points, but remains of order 10^{-3} elsewhere in the domain, including the subdomain containing the beam.

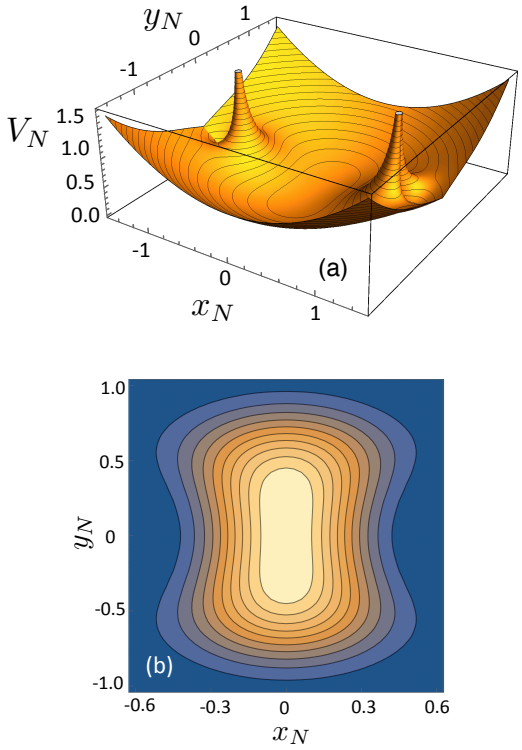

FIG. 3. (Upper, panel a) The potential (41), shown for $\tau = -0.4$. (Lower, panel b) Contours of the spatial projection P_{xy} of the thermal equilibrium phase space density f_{eq} obtained for a 2.5 MeV proton beam with current $I = 60.7$ mA in a constant focusing channel described by (39b).

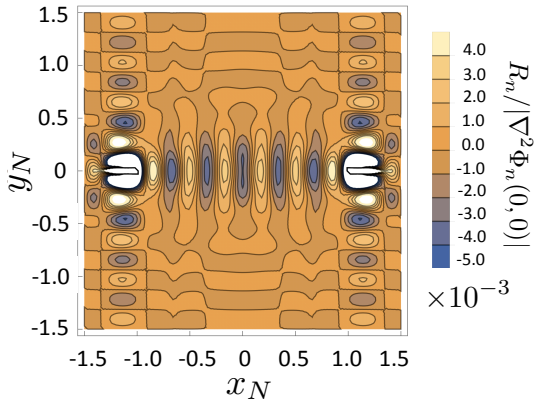

FIG. 4. Residual in the transverse plane for the numerical solution of (15) with the applied potential (39b) obtained using 15×15 modes. The result is given relative to the local maximum of $\nabla^2\Phi_n$ located at the origin $(x, y) = (0, 0)$.

To verify that the phase space density f_{eq} is a stationary solution of the Vlasov-Poisson system (2-6), a beam consisting of 1 M particles was sampled from f_{eq} and tracked self-consistently according to the Hamiltonian (39) using the code IMPACT-Z [20]. A second-order symplectic integrator [21] was used for numerical integration in s, with stepsize $\Delta s = 0.0014/k$. At each step in s, the solution of the Poisson equation (11) for the space charge potential Φ is obtained from the particle data at s using the gridless spectral algorithm described in [22]. In particular, Φ is computed at each step on the rectangular domain $(-a, a) \times (-b, b)$ as a linear combination of the basis functions (31), where a and b take the values provided above.

Figure 5 shows projections (profiles) of the particle density along each of the four phase space coordinates (x, p_x, y, p_y). The initial profiles coincide with the profiles obtained after tracking for distance $L = 2000/k$ (2.6 km) at the target current ($I = 60.7$ mA), demonstrating that the 4D phase space density is well-preserved. Note the depression appearing in the vertical beam profile near $y = 0$, which in this system is characteristic of Vlasov equilibria at high space charge intensity.

For comparison, Fig. 6 shows the result of tracking the same initial particle distribution over the same distance using the mismatched current value $I = 0$. After tracking, both the horizontal and vertical beam size are reduced, and the depression in the vertical beam profile has disappeared. These figures indicate clearly the importance of collective effects in determining a true Vlasov equilibrium at these beam and lattice parameters. More detailed studies of the dynamics of this system will be described in a future publication.

VII. CONCLUSIONS

A computational tool was developed for producing stationary solutions of the Vlasov-Poisson system describing a relativistic charged-particle beam in self-consistent equilibrium in a constant focusing channel, confined transversely by a general (linear or nonlinear) confining potential. The tool allows one to study the structure of beam equilibria in high-intensity accelerator systems at a specified value of beam current. Distinct families of beam equilibria can be studied by varying the function $\tilde{G}$, which describes the shape of the equilibrium density in the 4D phase space. The method utilizes a variation of the spectral Galerkin algorithm for solving a nonlinear PDE for the electrostatic potential describing the beam self-fields. A procedure for constructing exactly-soluble test problems was described, and applied to study numerical convergence. The code generates a particle distribution sampled from the 4D Vlasov equilibrium phase space density, and preservation of the density was confirmed for a challenging application using numerical tracking studies.

A large literature exists regarding the numerical solution of nonlinear PDEs of the form (16). The use of a spectral method involving Laplacian eigenfunctions is conceptually simple and robust, and it connects naturally with the Poisson solver described in [22]. However,

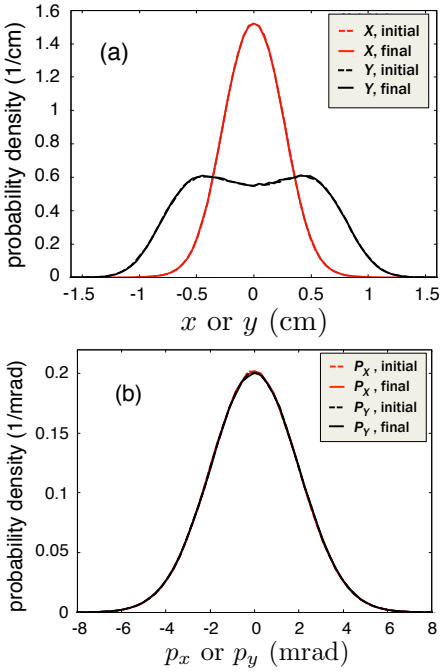

FIG. 5. Projected density profiles of a stationary 2.5 MeV proton beam with current $I = 60.7$ mA in a constant focusing channel described by (39b), shown before and after tracking a distance $L = 2000/k$. The curves obtained before and after tracking coincide. In (b), the two curves corresponding to p_x, initial and p_y, initial also coincide.

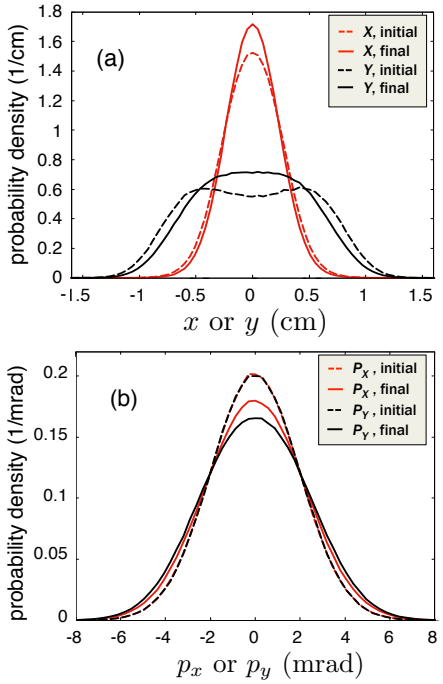

FIG. 6. Projected density profiles of a 2.5 MeV proton beam with the same initial phase space density as in Fig. 5, given before and after tracking a distance $L = 2000/k$ in the constant focusing channel (39b) at the unmatched current $I = 0$. Evolution of the density is evident. In (b), the two curves corresponding to p_x, initial and p_y, initial coincide.

we remark that alternative numerical methods exist that may yield improved numerical convergence [23], and the possibility of constructing Vlasov equilibria using these methods is also under consideration.

APPENDIX A: BEAM DISTRIBUTION TYPES

The purpose of this Appendix is to relate the notation of this paper to the existing literature on self-consistent beam equilibria, by describing four beam distribution types of special interest. In each example, the phase space density and spatial density are given by $f_{eq} = f_0 \tilde{G} \circ H$ and $P_{xy} = f_0 G_{\rm int} \circ V$, respectively, where f_0 is a normalization constant chosen such that (1) is satisfied. Here, H and V are the self-consistent Hamiltonian and potential, given by (3) and (9), respectively.

Type 1: To obtain a Kapchinskij-Vladimirskij (KV) distribution, one considers the limiting case when:

$$\tilde{G}(h) = \delta(H_0 - h), \qquad G_{\rm int}(h) = \Theta(H_0 - h), \tag{42}$$

where H_0 is a constant, δ is a Dirac-delta distribution, and Θ is a unit step function.

Type 2: To obtain a hard-edged waterbag distribution, one considers the limiting case when:

$$\tilde{G}(h) = \Theta(H_0 - h), \qquad G_{\rm int}(h) = (H_0 - h)\Theta(H_0 - h), \tag{43}$$

where H_0 characterizes the location of the outer beam edge in the 4D phase space.

Type 3: For numerical purposes, is useful to consider a soft-edged waterbag distribution, given by:

$$\tilde{G}(h) = \frac{1}{2}(1+\tanh(s)), \qquad G_{\rm int} = \frac{\lambda}{2} H_0 (s + \ln(2\cosh s)), \tag{44}$$

where $\lambda > 0$ is a parameter characterizing the width of the transition at the beam edge, and

$$s = \frac{H_0 - h}{\lambda H_0}. \tag{45}$$

Note that (44) converges to (43) as $\lambda \to 0$.

Type 4: To obtain a thermal (Boltzmann) distribution one takes:

$$\tilde{G}(h) = \exp(-h/H_0), \qquad G_{\rm int} = H_0 \exp(-h/H_0), \tag{46}$$

where H_0 characterizes the beam temperature:

$$H_0 = \frac{1}{2} \int (p_x^2 + p_y^2) f_{eq}(x, p_x, y, p_y) dx dp_x dy dp_y. \tag{47}$$

For the special case (46), equation (15) appears in the literature under the name of the Poisson-Boltzmann-Emden equation [24–26].

Numerical benchmarks of the code described in Sections 3-4 were performed using Types 3 and 4 above, for which the functions $\tilde{G}$ and $G_{\rm int}$ are smooth.

APPENDIX B: EXACTLY-SOLUBLE TEST PROBLEMS

Using the procedure described in Section V, we may construct an applied focusing potential V_0 such that the nonlinear PDE (15) possesses an exactly-known solution. In the following examples, we take $G_{\rm int}(h) = H_0 e^{-h/H_0}$ ($H_0 > 0$), and let the problem domain be $\Omega = (-a, a) \times (-b, b)$.

Problem I: Consider an applied potential of the form:

$$V_0^{(I)}(x,y) = -H_0 \log\left(1 - \frac{x^2+y^2}{a^2+b^2}\right) + C\left[1 - \left(1-\frac{x^2}{a^2}\right)\left(1-\frac{y^2}{b^2}\right)\right], \quad (48)$$

where the constant C is given by

$$C = \frac{3\Lambda}{32\pi}\left(\frac{ab}{a^2+b^2}\right). \quad (49)$$

Then the exact solution of the nonlinear PDE (15) using the applied potential (48) is given by the simple function:

$$\Phi_d^{(I)}(x,y) = C\left(1-\frac{x^2}{a^2}\right)\left(1-\frac{y^2}{b^2}\right), \quad (50)$$

with normalization constant

$$f_0^{(I)} = \frac{3e^{C/H_0}}{16\pi ab H_0}, \quad (51)$$

and the equilibrium beam density is given by:

$$f_{eq}^{(I)} = \frac{P_{xy}^{(I)}}{2\pi H_0}\exp\left(-\frac{||p||^2}{2H_0}\right), \quad (52)$$

with corresponding spatial density:

$$P_{xy}^{(I)}(x,y) = \frac{3}{8ab}\left(1-\frac{x^2+y^2}{a^2+b^2}\right). \quad (53)$$

The potential $V_0^{(I)}$ is minimum and vanishing at the origin. Note that $P_{xy}^{(I)}$ vanishes at the four corners of the domain boundary, and is strictly positive in Ω.

Problem II: As a second example, choose:

$$V_0^{(II)}(x,y) = -H_0 \log\left[\left(1-\frac{x^2}{a^2}\right)\left(1-\frac{y^2}{b^2}\right)\right] + \Phi_d^{(II)}(0,0) - \Phi_d^{(II)}(x,y) \quad (54)$$

where $\Phi_d^{(II)}$ is given by the convergent series:

$$\Phi_d^{(II)} = -\frac{\Lambda}{2\pi}\sum_{\substack{l,m=1\\ l,m \text{ odd}}}^{\infty}\frac{1}{\lambda_{lm}}\left(\frac{576}{l^3m^3\pi^6\sqrt{ab}}\right)e_{l,m}, \quad (55)$$

where the functions $e_{l,m}$ are given in (31a). Then the exact solution of (15) is given by (55), with normalization constant

$$f_0^{(II)} = \frac{9}{32\pi ab H_0}\exp\left(\frac{\Phi_d(0,0)}{H_0}\right), \quad (56)$$

and the equilibrium beam density is given by:

$$f_{eq}^{(II)} = \frac{P_{xy}^{(II)}}{2\pi H_0}\exp\left(-\frac{||p||^2}{2H_0}\right),$$

with corresponding spatial density

$$P_{xy}^{(II)}(x,y) = \frac{9}{16ab}\left(1-\frac{x^2}{a^2}\right)\left(1-\frac{y^2}{b^2}\right). \quad (57)$$

The potential $V_0^{(II)}$ is minimum and vanishing at the origin. Note that $P_{xy}^{(II)}$ vanishes everywhere on the domain boundary.

The exact value of the coefficient d appearing in the error estimate for this problem, which appears in (37b), is given by the sum:

$$d = \sum_{\substack{l,m=1\\ l,m \text{ odd}}}^{\infty}\frac{1}{(l^2+m^2)^2 l^6 m^6} \quad (58)$$

which is well-approximated by its first term, giving $d \approx 1/4$.

APPENDIX C: SUMMARY OF NOTATION

All functions are assumed to be real-valued unless otherwise specified. If an integral sign appears without limits, the integral is to be taken over the entire domain. The following notation is standard. If u, $v \in \mathbb{R}^d$, then we denote

$$\langle u, v\rangle = \sum_{j=1}^{d} u_j v_j, \qquad ||u|| = \langle u, u\rangle^{1/2}. \quad (59)$$

If g, h are real-valued functions on the domain $\Omega \subseteq \mathbb{R}^2$, then we denote

$$\langle g, h\rangle = \int_\Omega g(x,y)h(x,y)dxdy, \qquad ||g|| = \langle g, g\rangle^{1/2}, \quad (60)$$

and $L^2(\Omega)$ denotes the set of (measurable) functions $g : \Omega \to \mathbb{R}$ with $||g|| < \infty$. If $u_1, u_2, \ldots, u_n \in L^2(\Omega)$, then $\text{Span}\{u_1, \ldots, u_n\}$ denotes the set of all linear combinations of $u_1, \ldots, u_n$ with real coefficients. Finally, the notation $F(\cdot, U)$ is used to denote the function that maps

$$(x,y) \mapsto F(x,y,U(x,y)), \qquad (x,y) \in \Omega. \quad (61)$$

VIII. ACKNOWLEDGEMENTS

This work was supported by the Director, Office of Science of the U.S. Department of Energy under Contract No. DE-AC02-05CH11231, and made use of computer resources at the National Energy Research Scientific Computing Center. The authors acknowledge support from the U.S. DOE Early Career Research Program under the Office of High Energy Physics. Thanks to the IOTA collaboration teams at Fermilab and RadiaSoft for helpful discussions.

[1] M. Reiser, *Theory and Design of Charged Particle Beams*, 2nd ed, Wiley-VCH, Weinheim, 2008.
[2] R. Davidson and H. Qin, *Physics of Intense Charged Particle Beams in High Energy Accelerators*, Imperial College Press and World Scientific Publishing Co., London, 2001.
[3] S. M. Lund, T. Kikuchi, and R. C. Davidson, Phys. Rev. ST Accel. Beams **12**, 114801 (2009).
[4] J. Struckmeier and I. Hofmann, Particle Accelerators **39**, 219-249 (1992).
[5] S. I. Tzenov and R. C. Davidson, Phys. Rev. ST Accel. Beams **5**, 021001 (2002).
[6] I. M. Kapchinskij and V. V. Vladimirskij, *Proceedings of the International Conference on High Energy Accelerators*, CERN, Geneva, p. 274 (1959).
[7] I. Hofmann, Phys. Rev. E **57**, 4713 (1998).
[8] K. Sonnad and J. Cary, Phys. Plasmas **22**, 043120 (2015).
[9] R. Spencer, S. Rasband, and R. Vanfleet, Phys. of Fluids B: Plasma Physics **5**, 4267 (1993).
[10] K. Atkinson and W. Han, Electronic Transactions on Numerical Analysis **17**, 206-217 (2004).
[11] K. Atkinson and A. Sommariva, Computing **74**, 159-175 (2005).
[12] M. Einsiedler and T. Ward, *Functional Analysis, Spectral Theory, and Applications*, Springer International Publishing, Gewerbestrasse, Switzerland (2017), **Theorem 6.56**.
[13] J. Neuberger and J. Swift, Int. Journal of Bifurc. and Chaos **11**, 801 (2001).
[14] M. Badiale and E. Serra, *Semilinear Elliptic Equations for Beginners: Existence Results via the Variational Approach*, Springer-Verlag, London (2011).
[15] C. G. Broyden, Math. Comp. **19**, 577-593 (1965).
[16] W. Press *et al*, *Numerical Recipes in Fortran*, 2nd ed., Cambridge University Press, 1992, **Sect. 9.7**.
[17] A. H. Stroud, *Approximate Calculation of Multiple Integrals*, Prentice-Hall, Englewood Cliffs, NJ, 1971.
[18] V. Danilov and S. Nagaitsev, Phys. Rev. ST Accel. Beams **13**, 084002 (2010).
[19] S. Antipov *et al*, Journal of Instrumentation **12**, T03002 (2017).
[20] Ji Qiang, R. Ryne, S. Habib, and V. Decyk, Journal of Computational Physics **163**, 434-451 (2000).
[21] C. Mitchell and J. Qiang, "Numerical Tools for Modeling Nonlinear Integrable Optics in IOTA with Intense Space Charge Using the Code IMPACT-Z," in Proc. IPAC2018, THPAK035, Vancouver, BC, Canada, 2018.
[22] Ji Qiang, Phys. Rev. Accel. Beams **20**, 014203 (2017).
[23] K. Atkinson, D. Chien, and O. Hansen, Numerical Algorithms **74**, 797-819 (2017).
[24] F. Bavaud, Rev. Mod. Phys. **63**, 129 (1991).
[25] J. Dolbeault, J. Math. Pures Appl. **78**, 121 (1999).
[26] F. Bouchut and J. Dolbeault, Differential and Integral Equations **8**, 487 (1995).